

Pore-scale modelling of relative permeability of cementitious materials using X-ray computed microtomography images

Mingzhong Zhang^{*}

Advanced and Innovative Materials (AIM) Group, Department of Civil, Environmental and Geomatic Engineering, University College London, London WC1E 6BT, UK

Abstract: Permeability of cementitious materials is an important durability indicator. In practice, concrete is rarely saturated. Therefore, it is essential to study permeability of unsaturated cementitious materials. This paper presents an integrated modelling approach for estimating permeability of cementitious materials over the full range of saturation. An in-house code based on multiphase and single-phase lattice Boltzmann models is developed and used to simulate the moisture distribution and fluid flow in unsaturated cement paste with various curing ages, the 3D microstructures of which are obtained from X-ray micro-CT. The water permeability and gas permeability of partially saturated cement paste are then estimated. The results indicate with decreasing water saturation water permeability decreases while gas permeability increases. Additionally, the moisture distribution and permeability of unsaturated cement paste are strongly dependent on its microstructure. Moreover, there exists a unique relationship between permeability and effective porosity. The simulation results show good agreement with experimental data.

Keywords: Permeability (C); Cement paste (D); Microstructure (B); Pore size distribution (B); Lattice Boltzmann method

1. Introduction

Concrete is a composite material primarily composed of aggregate, cement and water. It is the most widely used man-made material in the world. The cement, commonly Portland cement and other cementitious materials such as fly ash and slag cement, serve as a binder for the aggregate. In recent years, durability of concrete has become a main concern for safety, economic and environmental

* Corresponding author. Tel: +44 (0)20 7679 7299. E-mail address: mingzhong.zhang@ucl.ac.uk (M. Zhang)

reasons. It is well known that durability issues, such as chloride-induced corrosion of reinforcing steel, carbonation, freeze-thaw action and so on are closely associated with fluid and ion transport in cementitious materials. As such, fluid permeability (e.g. water permeability and gas permeability) of cementitious materials is considered as an important indicator to evaluate the durability and predict the service life of reinforced concrete structures [1]. In practice, concrete is rarely in a state of full saturation during construction and throughout its long lifetimes due to self-desiccation and wetting-drying cycles [2]. In addition, the corrosion of reinforcing steel in concrete occurs only in an unsaturated state, whereby the oxygen can get access to the rebar surface. Therefore, it is vital to estimate permeability of partially saturated cementitious materials in order to make an accurate prediction of service life and assessment of durability of reinforced concrete structures.

Because of its scientific interests and practical importance, permeability of unsaturated cementitious materials has been recently receiving growing attention. In the last few years, an increasing number of efforts have been made to experimentally, analytically and numerically investigate the influence of degree of water saturation on permeability of cementitious materials. However, it should be noted that to date only a limited amount of results have been presented.

With respect to experimental studies, Abbas et al. [3] measured the oxygen permeability of cementitious materials with various moisture contents between the saturated state and perfectly dry using the CEMBUREAU apparatus. The cylindrical specimens with 15 cm in diameter and 5 cm in thickness were prepared and used for testing. The measured value of oxygen permeability of cementitious materials not only depended strongly on its degree of saturation but varied with the applied pressure. Galle and Daian [4] carried out gas permeability tests on unsaturated hardened cement pastes prepared with CEM I and CEM V cement with water-to-cement (w/c) ratios of 0.3, 0.4 and 0.5 and reported that the gas permeability of cement pastes was significantly influenced by degree of water saturation and microstructural characterisations of the specimens, such as porosity and pore size distribution. The relationship between gas permeability and degree of water saturation followed a nonlinear regression. The evolution of water and gas permeability of partially saturated cementitious

materials was tested in [5-7]. The relative water permeability (i.e., the ratio between the water permeability measured at a given saturation and that at fully saturated state) and relative gas permeability (i.e., the ratio between the gas permeability measured at a given saturation and that at fully dry state) were defined and determined as a function of water saturation to quantify the effect of water saturation on permeability of cementitious materials. The experimental results all showed that the water and gas permeability strongly depended on the degree of saturation. In addition, a drastic influence of saturation was observed on the relative permeability of water and gas. Zamani et al. [8] reported measurements of the permeability of cement paste as a function of relative humidity using magnetic resonance profiling and found that the permeability of cement paste was strongly relative humidity dependent. Note that the tests are usually time-consuming taking from several weeks to several months or even longer. Moreover, it is still a challenging task to obtain and maintain a desired degree of water saturation of the specimens during the tests [2].

As to analytical studies, the Mualem model [9] and the Van Genuchten model [10] were the two most widely used analytical expressions to describe permeability of unsaturated porous media, e.g., soils and cementitious materials, as a function of degree of saturation. Based on a series of experimental results, Monlouis-Bonnaire et al. [6] and Wardeh and Perrin [7] proposed a modified Van Genuchten model, which was subsequently validated by Baroghel-Boundy [11]. Recently, some general analytical models for fluid permeability of cementitious materials against degree of saturation were derived from conductivity theory and proposed by Zhou [12] and Zhou et al. [13, 14]. It is worth mentioning that most of these analytical models are semi-empirical expressions by fitting the limited experimental data. A further validation of these models with more experiments is required before their applications.

In regard to numerical studies, Martys [15] is the pioneer to introduce lattice Boltzmann (LB) method into the field of transport properties prediction for partially saturated cementitious materials. Martys and Hagedorn [16] used a single-phase multi-component LB model to simulate the distribution of wetting fluid (e.g. liquid) and non-wetting fluid (e.g. gas) and the relative fluid

permeability in a sandstone. It was observed that there was a significant dependence of fluid permeability on degree of saturation. However, the used LB model is only available for the liquid–gas mixture with a density ratio of less than 58 [17]. The water–gas system whose density ratio is approximately $1000/1.29 = 775$ is beyond the capacity of this model. In recent years, Zalzale and McDonald [18], Zalzale et al. [19] and Li et al. [20] studied the liquid water permeability and gas permeability of partially saturated cement paste using LB method and discrete element method, respectively, and found that the relative permeability values of cement paste were not only dependent on degree of saturation but also on three-dimensional (3D) microstructure of cement paste. However, it should be mentioned that the 3D microstructures used in [19, 20] were virtual microstructures generated by computer-based models, which might not be able to well represent the real microstructures of cement paste and need further validation. In addition, a prescribed degree of water saturation was simulated by removing a specific amount of water from the large pores in the virtual pore structure of cement paste, which is rather arbitrary and far from accurate, as the distribution of liquid and gas in cement paste at a certain degree of water saturation depends not only on the pore size but also on other microstructural characteristics, e.g., connectivity of pore network and morphology of solid surface [21]. Furthermore, the used LB model in [19] is a single-relaxation-time (SRT) model, which has been proved to be viscosity-dependent, i.e., the dependence of simulation results on the selected relaxation time, an input parameter for LB simulations [17, 22].

The main purpose of this paper is to present a pore-scale modelling of water permeability and gas permeability of cement paste with various levels of water saturation accounting for microstructural details. The 3D microstructures of hardened cement paste with curing ages of 1, 7 and 28 days were obtained from high-resolution X-ray computed microtomography (micro-CT) along with a series of image processing. A modified multiphase LB model is developed and applied to simulate the interactions between liquid, gas and solid phases and subsequently acquire the equilibrium distribution of moisture (a mixture of liquid and gas) in 3D pore structure of cement paste at different degrees of water saturation. Afterwards, a single-phase multiple-relaxation-time (MRT) model,

which can effectively overcome the drawbacks of SRT model, is implemented and used to simulate the fluid flow (e.g. water and gas) through cement paste over the full range of water saturation and obtain the corresponding water permeability and gas permeability of cement paste. Thus, the influences of both degree of water and saturation and 3D microstructure on permeability of partially saturated cement paste are investigated in a quantitative manner, the results of which are compared with available experimental data in the literature.

2. 3D microstructure of cement paste obtained from X-ray micro-CT

2.1 X-ray micro-CT images

X-ray micro-CT is a non-destructive technique that allows the visualisation of the internal structure of a sample in three dimensions. In this work, the 3D microstructure of cement paste was obtained from X-ray micro-CT scans. ASTM type I Portland cement was used. The w/c ratio of the cement paste was 0.5 (mass ratio). After drill mixing in a plastic beaker, small parts of the paste were poured into the syringe and then injected into a micro plastic tube with an internal diameter of 250 μm . The specimen was stored in the standard curing room with a relative humidity of 95% and temperature of 20 °C and scanned at 1, 7 and 28 days. A high resolution Xradia MicroXCT-200 CT scanner at the Beckman Institute for Advanced Science and Technology at the University of Illinois at Urbana-Champaign was used for acquiring projection images with a spatial resolution of 0.5 μm . The image reconstruction was performed using the algebraic method implemented in the Xradia reconstruction software that results in a 3D stack of virtual 8-bit cross-section images with grayscale values from 0 to 255. More details about the X-ray micro-CT testing can be found in [23].

A cylindrical region of interest (ROI) with 200 μm in diameter and 100 μm in thickness was extracted from the centre of the reconstructed 3D images where the cement paste is considered to be most homogeneous. Fig. 1 shows the micro-CT grey images of ROI of cement paste with curing ages of 1, 7 and 28 days, respectively. The dark phase represents capillary pores. The white phase stands for anhydrous cement grains. The grey phases most likely correspond to hydration products. The hydration of cement proceeds with increasing curing age, as a result of which cement (i.e. white phase)

and water (i.e. dark phase) are continuously consumed and an increasing number of hydration products (i.e. grey phase) appear in cement paste. In order to identify these three phases in cement paste, i.e., capillary pore, hydration product and anhydrous cement grain, and quantify their volume fractions, a series of image processing and analysis are required, the details of which are given below.

Fig. 1 Micro-CT images of hydrating cement pastes with 200 μm in diameter and 100 μm in thickness with curing ages of (a) 1 day; (b) 7 days; (c) 28 days. The dark, grey and white phases represent capillary pore, hydration product and anhydrous cement grain, respectively

2.2 Microstructural characteristics

Based on the grey-level histogram of micro-CT images, the global thresholding method is applied and implemented by using ImageJ to determine two threshold grey values to segment pores from anhydrous cement grains and hydration products, and subsequently segment anhydrous cement grains from hydration products, respectively. As a result, the original grey scale image is converted into a ternary image composed of capillary pore, anhydrous cement grain and hydration product. Fig. 2 shows the segmented capillary pore and anhydrous cement grain in 7-day old cement paste corresponding to the original image in Fig. 1b. With this ternary image, the microstructural characteristics of cement paste, in particular, pore structural features, such as porosity, pore size distribution, connectivity and tortuosity of the pore network, can be obtained in a quantitative manner after a series of image analysis. The reader is referred to [24, 25] for further information on image processing and analysis. Here special emphasis is only placed on the porosity, pore size distribution and 3D microstructure of volume of interest (VOI) of cement paste with various curing ages.

The porosity of cement paste at 1, 7 and 28 days is found to be 27.3%, 18.9% and 13.5%, respectively. It should be pointed out that the individual phase with size less than 0.5 μm cannot be identified separately due to the limited spatial resolution of micro-CT, i.e. 0.5 μm . Therefore, some pores smaller than 0.5 μm would not be counted into the porosity here, as a result of which the

porosity values obtained from micro-CT images is generally less than those measured by means of conventional techniques, e.g., mercury intrusion porosimetry (MIP). For a detailed discussion about the comparison between the porosity values determined using micro-CT, MIP and Power's model, see Zhang et al. [23]. As curing age increases, the porosity of cement paste decreases. Fig. 3 shows the obtained pore size distribution of cement paste with curing ages of 1, 7 and 28 days. It can be observed that pore size is reduced with increasing curing age due to the progress of cement hydration. In addition, cement paste at 1 day contains more big pores compared to 7 and 28-day old cement pastes. The representative elementary volume (REV) for transport properties of cement paste was found to be $100 \times 100 \times 100 \mu\text{m}^3$ [26]. Therefore, a cubic volume of interest (VOI) of $100 \times 100 \times 100 \mu\text{m}^3$ was extracted from the centre of ROI for following simulations. The 3D microstructure and pore structure of VOI of cement paste with curing ages of 1 day and 7 days are shown in Fig. 4.

Fig. 2 Different phases in 7-day old cement paste: (a) Anhydrous cement grains; (b) Capillary pores

Fig. 3 Pore size distribution of cement paste with curing ages of 1, 7 and 28 days

Fig. 4 Hardened cement paste with $100 \times 100 \times 100 \mu\text{m}^3$: (a) Microstructure at 1 day; (b) Pore structure at 1 day; (c) Microstructure at 7 days; (d) Pore structure at 7 days. Red, light grey and blue regions denote anhydrous cement grain, hydration product and capillary pore, respectively

3. Lattice Boltzmann method

3.1 General lattice Boltzmann model

The LB method is a recently developed numerical scheme based on microscopic particle dynamics that provides solutions to macroscopic hydrodynamics. In LB method, the physical and velocity space is discretized into a regular lattice of nodes and a set of microscopic velocity vectors, respectively.

Each lattice node contains a particle distribution function, $f_i(\mathbf{x}, t)$, in which i is the index of each velocity direction, \mathbf{x} is the location of the lattice node and t is time. Fluids are modelled as swarms of streaming and colliding particles. The evolution of particle distribution functions in time can be given according to the discrete LB equation:

$$f_i(\mathbf{x} + \mathbf{e}_i \Delta t, t + \Delta t) - f_i(\mathbf{x}, t) = \Omega_i \quad (1)$$

where Ω_i stands for the collision operator, which can be described using the SRT and MRT approximation. The left-hand side of the equation represents the streaming of particles by passing the particle distribution at each node to its neighbouring nodes. The right-hand side denotes the collision of particles.

The LB equation with SRT scheme for each lattice velocity is described as [27]

$$f_i(\mathbf{x} + \mathbf{e}_i \Delta t, t + \Delta t) - f_i(\mathbf{x}, t) = -\frac{1}{\tau} [f_i(\mathbf{x}, t) - f_i^{eq}(\mathbf{x}, t)] \quad (2)$$

where f_i and f_i^{eq} are the non-equilibrium and equilibrium particle distribution functions at location \mathbf{x} at time t , τ is the relaxation time which is related to the kinematic viscosity of fluid (v) as $v = c_s^2(\tau - 0.5)$ with sound speed or propagation speed of $c_s^2 = 1/3(\Delta x/\Delta t)^2$, herein, the lattice-spacing Δx and time-step Δt are defined as 1 lu and 1 ts (lu and ts refer to lattice units and time step respectively in the LB method), \mathbf{e}_i is the microscopic velocity at location \mathbf{x} at time t . For 3D LB simulations, the most widely used lattice model is D3Q19 (see Fig. 5), in which the 3D discrete phase space is defined by a cubic lattice with 19 discrete particle velocities as

$$\mathbf{e}_i = \begin{bmatrix} 0 & 1 & -1 & 0 & 0 & 0 & 0 & 1 & 1 & 1 & 1 & 0 & 0 & -1 & -1 & -1 & -1 & 0 & 0 \\ 0 & 0 & 0 & 1 & -1 & 0 & 0 & 1 & -1 & 0 & 0 & 1 & 1 & 1 & -1 & 0 & 0 & -1 & -1 \\ 0 & 0 & 0 & 0 & 0 & 1 & -1 & 0 & 0 & 1 & -1 & 1 & -1 & 0 & 0 & 1 & -1 & 1 & -1 \end{bmatrix} \quad (3)$$

For the D3Q19 model, the equilibrium particle distribution function f_i^{eq} is given by

$$f_i^{eq} = w_i \rho \left[1 + \frac{\mathbf{e}_i \cdot \mathbf{u}}{c_s^2} + \frac{(\mathbf{e}_i \cdot \mathbf{u})^2}{2c_s^4} - \frac{\mathbf{u} \cdot \mathbf{u}}{2c_s^2} \right] \quad (4)$$

where ρ and \mathbf{u} are the macroscopic density and velocity respectively, w_i is the weight factor associated with the i^{th} direction which is given as $w_i = 1/3$ ($i = 0$), $w_i = 1/18$ ($i = 1, 2, \dots, 6$) and $w_i =$

$1/36$ ($i = 7, 8, \dots, 18$). The local macroscopic properties, such as total density (mass) ρ , total velocity \mathbf{u} and pressure p of each lattice node can be obtained from the particle distribution function as follows

$$\rho = \sum_{i=0}^{18} f_i, \quad \mathbf{u} = \frac{1}{\rho} \sum_{i=0}^{18} (f_i \mathbf{e}_i), \quad p = c_s^2 \rho \quad (5)$$

Fig. 5 Lattice velocity direction of the D3Q19 lattice Boltzmann model

3.2 Single-phase multi-relaxation-time lattice Boltzmann model

The simplicity of SRT model has motivated its widespread use. However, this model has two significant drawbacks: numerical instability and the so-called viscosity dependence, i.e., the dependence of permeability of porous media on the used relaxation time τ [17]. These inherent shortcomings can be drastically reduced by using MRT collision scheme [17]. In this work, an in-house 3D LB code, PermLBS, based on the MRT model proposed by d'Humières et al. [28] was developed to simulate single-phase fluid (e.g., water and gas) permeation through porous media, e.g., cementitious materials. A brief introduction to this model is given below.

The essential difference between the SRT model and MRT model is the collision operator Ω_i in Eq. 1. The collision operator of MRT model is given by

$$\Omega_i = -M^{-1} \hat{S} [\mathbf{m}_i(\mathbf{x}, t) - \mathbf{m}_i^{eq}(\mathbf{x}, t)] \quad (6)$$

where the collision matrix $\hat{S} = MSM^{-1}$ is a diagonal relaxation matrix, the transformation matrix M relates the distribution functions f and f^{eq} to their moments \mathbf{m} and \mathbf{m}^{eq} as

$$\mathbf{m} = Mf, \quad \mathbf{m}^{eq} = Mf^{eq} \quad (7)$$

where the transformation matrix M can be constructed from the monomials of Cartesian components of the discrete velocities by applying the Gram-Schmidt orthogonalization procedure [28]. The row vectors of M are mutually orthogonal, i.e., $M^{-1}M^T$ is a diagonal matrix, but not normalized, so that its matrix elements are integers.

For D3Q19 model, the values of diagonal relaxation matrix \hat{S} composed of a series of relaxation rates is defined as

$$\begin{aligned}\hat{S} &= \text{diag}(s_0, s_1, s_2, s_3, s_4, s_5, s_6, s_7, s_8, s_9, s_{10}, s_{11}, s_{12}, s_{13}, s_{14}, s_{15}, s_{16}, s_{17}, s_{18}) \\ &= \text{diag}(0, s_e, s_\varepsilon, 0, s_q, 0, s_q, s_v, s_\pi, s_v, s_\pi, s_v, s_v, s_v, s_m, s_m, s_m)\end{aligned}\quad (8)$$

The relaxation rate s_v is related to the kinematic viscosity of the fluid as

$$s_v = \frac{2}{6\nu+1} = \frac{1}{\tau} \quad (9)$$

The remaining relaxation rates, i.e., s_e , s_ε , s_q , s_π and s_m can be freely chosen within the range from 0 to 2 and can be adjusted to improve the accuracy as well as the stability of the MRT model. A good choice of these relaxation rates for stokes flow is given by Eq. 10. The optimal values of \hat{S} and M and the transformations of \mathbf{m}^{eq} for D3Q19 model can be found in [28].

$$s_e = s_\varepsilon = s_\pi = s_v, \quad s_q = s_m = 8 \frac{2-s_v}{8-s_v} \quad (10)$$

The SRT model is actually a special case of MRT model, in which the relaxation rates are all equal and set to $1/\tau$. However, the tunable relaxation rates in MRT model provide several advantages and wider application over SRT model. The implementation of MRT model is straightforward, which consists of two main steps: collision and streaming. The collision step is to calculate the distribution function components in Eq. 2 as $f_i^*(\mathbf{x}, t) = f_i(\mathbf{x}, t) + \Omega_i$ and the streaming step is to propagate $f_i^*(\mathbf{x}, t)$ to the neighbouring nodes and generate the non-equilibrium distribution function for the next time step as $f_i(\mathbf{x} + \mathbf{e}_i \Delta t, t + \Delta t) = f_i^*(\mathbf{x}, t)$. After this, the density and velocity at each lattice node are updated using Eq. 5. In order to validate the PermLBS module, three benchmark tests including the 3D Poiseuille flow in a square channel, flow through a body-centred cubic array of spheres and a random sphere packing were performed, the results of which show good agreement with the analytical solutions. The reader is referred to [22] for more details.

3.3 Modified Shan-Chen multiphase lattice Boltzmann model

In order to obtain an accurate moisture distribution and to estimate permeability in partially saturated cement-based materials, it is essential to simulate the multiphase flow. In this work, the Shan-Chen (SC) multiphase model [29] that is one of the most commonly used multiphase models due to its simplicity, ease of implementation and remarkable versatility [30] is chosen and modified in order to simulate the high-density ratio multiphase system like liquid-gas system with a density ratio of about 775 at 20 °C and variable wettability, i.e., contact angle of the liquid/gas to the solid surface. The modified SC model is briefly introduced below. Based on this model, an in-house code, SCMLBS, was established and implemented in three dimensions to simulate the moisture distribution in cementitious materials.

The SC model extends from the single-phase LB model to take into account the fluid-fluid interaction force F_{int} , fluid-solid adhesion force F_{ads} and external force F_g including gravity effects by varying the macroscopic velocity of lattice nodes in Eq. 5 with the following equation

$$\mathbf{u} = \frac{1}{\rho} \sum_{i=0}^{18} (f_i \mathbf{e}_i) + \frac{\tau (F_{int} + F_{ads} + F_g)}{\rho} \quad (11)$$

Microscopically, the separation between two phases is the result of fluid-fluid interaction force. In the SC model, the fluid-fluid interaction force F_{int} between the fluid particles at lattice location \mathbf{x} and its closest neighbouring nodes at time step t is given by [29]

$$F_{int} = -G\psi(\mathbf{x}, t) \sum_{i=0}^{18} w_i \psi(\mathbf{x} + \mathbf{e}_i \Delta t, t) \mathbf{e}_i \quad (12)$$

where G is the coefficient of the attractive forces between fluid particles which represents the intensity of the interparticle interaction, ψ is the so-called “effective mass” which is a function of local density $\psi(\rho)$. The value of G is negative for attraction and positive for repulsion between particles. Increasing G within the critical value will lead to a tendency towards phase separation and a sharper interface. The “effective mass” function ψ directly relates to the interaction force. The forms of ψ control the detailed nature of the interaction potential and determine the equation of state (EOS) of the fluid system. In the SC model, ψ and EOS are written as [31]

$$\psi(\rho) = \sqrt{\frac{2(p - c_s^2 \rho)}{c_s^2 g}} \quad (13)$$

$$p = c_s^2 \rho + \frac{c_s^2 g}{2} \psi(\rho)^2 \quad (14)$$

It was found that the original SC model is only applicable to the liquid-gas system with a density ratio of less than 58, however, this drawback can be overcome by replacing the SC EOS with Carnahan-Starling (C-S) EOS described as [32]

$$p = \rho R_0 T \frac{1 + b\rho/4 + (b\rho/4)^2 - (b\rho/4)^3}{(1 - b\rho/4)^3} - a\rho^2 \quad (15)$$

with $a = 0.4693R_0^2T_c^2/p_c$, $b = 0.18727R_0T_c/p_c$. In simulations, the constants of a , b and R_0 are generally set to 1, 4 and 1, respectively [32].

Following the recommendations of [33], the adhesion force between liquid/gas phase and solid phase in the SC model F_{ads} can be modified and given by

$$F_{ads} = -G\psi(\mathbf{x}, t) \sum_{i=0}^{18} w_i \psi(\rho_w) s(\mathbf{x} + \mathbf{e}_i \Delta t) \mathbf{e}_i \quad (16)$$

where ρ_w is the virtual density of the solid phase which is a free parameter applied to denote different wettability, $s(\mathbf{x} + \mathbf{e}_i \Delta t)$ is an indicator function which is set to 1 if the neighbouring lattice site $(\mathbf{x} + \mathbf{e}_i \Delta t)$ is a solid node and to 0 otherwise. The adhesion force emerges once the neighbouring node of a fluid node is solid. By varying the value of ρ_w , the different contact angle between fluid and solid surface can be obtained conveniently.

In order to validate the SCMLBS module based on the modified SC model, two benchmark tests including bubble tests and contact angle test were carried out, which indicate that the SCMLBS module has the capacity to simulate the realistic multiphase flow phenomena, such as liquid-gas phase segmentation and variable wettability. Detailed information about the validation of SCMLBS can be found in previous work [21].

4. Modelling and simulation

The entire modelling procedure for relative permeability of cement-based materials consists of three main steps: mapping of 3D microstructure onto a discrete lattice, modelling of equilibrium distribution of moisture using modified SC multiphase model and modelling of water and gas permeability using single-phase MRT model. Each step is explained in detail below.

4.1 Mapping of 3D microstructure onto a discrete lattice

For LB simulation of fluid flow, an important consideration is the size of each lattice, which should be optimally as small as possible accounting of computing resources allow. Besides the computing resource limits and time constrictions, the determination of lattice size also depends on the 3D microstructure in order to adequately represent flow in a porous medium. In this study, the segmented micro-CT images of VOI of cement paste are mapped onto a discrete cubic lattice with a 1-to-1 correlation of voxel-to-node. As such, the 3D microstructure of cement paste ($100 \times 100 \times 100 \mu\text{m}^3$) is converted into a $200 \times 200 \times 200$ cubic lattice. The capillary pore voxels are considered as fluid nodes. The solid voxels composed of hydration products and anhydrous cement grains are regarded as impermeable solid nodes. The solid voxels in contact with pore voxels are considered to be bounce-back nodes, which act as algorithmic devices that return incoming streamed particle densities with the opposite momentum, producing a no-slip boundary condition halfway between the fluid and bounce-back nodes [34].

Besides the geometry mapping, it is essential to establish a corresponding mapping between the lattice units and real physical units: $xL_0 \rightarrow x_p$ (length), $tT_0 \rightarrow t_p$ (time) and $\rho M_0 \rightarrow \rho_p$ (mass), in which variables (x, t, ρ) are lattice units and (x_p, t_p, ρ_p) denote physical units. The length mapping L_0 is determined from the chosen resolution in the simulation. Here, the resolution $\Delta x_p = 0.5 \mu\text{m} = 5 \times 10^{-7} \text{ m}$. Since a lattice spacing $\Delta x = 1$, hence, $L_0 = \Delta x_p / \Delta x = 5 \times 10^{-7} \text{ m}$. The mass mapping is deduced from the fluid density. For example, the density of water at 20 °C is given as $\rho_{p,w} = 1000 \text{ kg/m}^3$. In the simulation, the density at all lattice nodes is set to $\rho = 1$. Since density has dimensions $[\text{M}][\text{L}]^{-3}$, $\rho_{p,w} = M_0 L_0^{-3} \rho$, hence, $M_0 = 1.25 \times 10^{-16} \text{ kg}$. The time mapping T_0 can be obtained from the user's choice of fluid kinematic viscosity $v_{p,w}$. For water at 20 °C, $v_{p,w} = 1.004 \times 10^{-6} \text{ m}^2/\text{s}$. It

has dimensions $[L]^2[T]^{-1}$. From the dimensions of fluid kinematic viscosity, it can be deduced that $\nu_{p,w} = \nu L_0^2/T_0$. In the LB model, the lattice viscosity ν is related to the relaxation time τ and the sound speed c_s according to $\nu = c_s^2 \cdot (\tau - 0.5)$. Suppose that $\tau = 1$, we can get $\nu = 1/6$, hence, $T_0 = 4.15 \times 10^{-8}$ s. With these unit conversions, the LB simulation results can be related to any quantities in the physical system, for example, velocity from lattice-spacing per time-step (lu/ts) in the simulation matches to meter per second (m/s) in the physical system.

4.2 Modelling of equilibrium distribution of moisture

The SCMPLBS module based on the modified SC multiphase LB model is used to simulate the liquid-gas and liquid/gas-solid interactions, and to establish the equilibrium distribution of moisture (i.e., a mixture of liquid and gas phases) in cement paste with various degrees of water saturation. At the beginning, the fluid nodes in the cubic lattice are saturated with a random homogeneous mixture of liquid and gas phases with a specific volume ratio that corresponds to a given degree of water saturation, S_w . Fig. 6 shows an example of the initial random distribution of moisture at $S_w = 50\%$ and $S_w = 72\%$ in 7-day old cement paste, the microstructure of which is shown in Fig. 4. Afterwards, a set of parameters, e.g., T and ρ_w as explained in Section 3.3, need to be determined for LB simulation of fluid flow in cementitious materials. The physical density ratio between liquid and gas is $1000/1.29 = 775$. Therefore, a suitable value for T , present in Eq. 15, should be chosen in order to meet the requirement of such density ratio of water and gas in lattice units. As shown in the bubble test for a liquid-gas system [21], a value of $T = 0.585$ yields a density ratio of liquid and gas phases of $0.4152/0.00053 = 783$. So, the initial liquid and gas densities in LB units are set to be 0.4152 and 0.00053, respectively. In addition, it is commonly assumed that the contact angle between liquid and solids in cementitious materials is zero. For this reason, the virtual density of solid nodes ρ_w , present in Eq. 16, is set to be close to the density of liquid phase, which leads to a zero contact angle, i.e., the solid phase is completely wetted by liquid [21].

At each time iteration, the system proceeds in three substeps. First, the particle distributions are streamed to respective nodes. On the pore-solid interface, the half-way no-slip bounce-back boundary

condition [34] is imposed, as a result of which the distribution functions from the fluid node streaming to their neighbouring solid nodes scatter back to the fluid node along its incoming direction. Second, the macroscopic density and velocity are determined from these new particle distributions, and when present, with the inclusion of an exterior force as stated in Section 3.3. Third, the equilibrium particle distribution is obtained and the particle distribution undergoes collision. The interaction between liquid, gas and solid phases is assumed to have reached an equilibrium state once the relative difference of the macroscopic density of liquid phase in the system at time step t and ($t-1000$) calculated by Eq. 5 is less than 10^{-5} .

Afterwards, the obtained equilibrium distribution of liquid and gas phases in cement paste with various degrees of water saturation is considered as the initial condition for the estimation of connectivity of liquid-filled and gas-filled pores, which is carried out using the in-house Perc3d module based on cluster-labelling algorithm [23]. On one hand, each gas voxel is converted to a solid-like voxel resulting in a new domain that consists of liquid-filled pore voxels, solid-like voxels and solid voxels. Using the Perc3d module, the connected and isolated liquid-filled pore voxels in the new domain are identified, based on which the connectivity of liquid-filled pores under various saturation degrees is quantified. Moreover, the critical degree of water saturation at which the liquid-filled pores become disconnected can be obtained. On the other hand, the connectivity of gas-filled pores is estimated in the same way by converting each water voxel to a solid-like voxel.

Fig. 6 Initial random distribution of liquid and gas phases in pore structure of 7-day old cement paste: (a) $S_w = 50\%$; (b) $S_w = 72\%$. Blue and grey phases represent liquid and gas, respectively

4.3 Modelling of water/gas permeability

Once the equilibrium distribution of liquid and gas phases in partially saturated cement paste is obtained, the LB simulation of permeability can be conducted using the PermLBS module. In the simulation, a pressure (density) difference is applied at the inlet and outlet sides in the z -direction to

drive the flow, which is dealt with using the non-equilibrium bounce-back rule proposed by Zou and He [35]. The other four sides are considered as periodic boundaries so that the nodes of opposite boundaries are treated as neighbouring. As such, the particle distributions moving out the domain from one side will re-enter the domain through its opposite side during the streaming step. The half-way no-slip bounce-back boundary condition is applied to the pore-solid interface.

The simulation is run until the steady-state flow condition is reached. The steady-state flow criterion is defined such that the difference in the average velocity of the whole domain between two consecutive time steps is less than a specified threshold value. This threshold value is selected to be 1.0×10^{-7} , which was found not only sufficient to guarantee the computational accuracy but also helpful to reduce the computing time and memory requirements. Once the steady-state flow condition is achieved, the flow velocity distribution within cement paste with various saturation levels can be acquired and the corresponding water/gas permeability can be calculated according to Darcy's law and written in terms of LB parameters as follows

$$\kappa_{lb} = \frac{\nu \langle u_z \rangle}{\nabla p} = \nu \cdot \frac{N_z \cdot \Delta x}{c_s^2 \cdot \Delta \rho} \cdot \frac{1}{N_x \cdot N_y \cdot N_z \cdot \delta x^3} \sum_{i=1}^{N_x} \sum_{j=1}^{N_y} \sum_{k=1}^{N_z} u_z(i, j, k) \quad (17)$$

where κ_{lb} is the intrinsic permeability in LB units, ν is the kinematic viscosity of fluid, $\langle u_z \rangle$ represents the overall mean value of velocity in the z -direction, ∇p is the pressure gradient, $\Delta \rho$ denotes the density difference between the inlet and outlet, N_x , N_y and N_z are the numbers of lattice node in the x , y and z -direction, respectively. Here, $N_x = N_y = N_z = 200$.

In the physical system, the intrinsic permeability of a porous material, κ , has dimensions of length squared. Using the unit conversion as described above, the intrinsic permeability in physical units can be derived from that in LB units, i.e., κ_{lb} , according to the relation $\kappa = \kappa_{lb} L_0^2$. If the fluid is water, the intrinsic permeability can be converted into saturated water permeability k_w (m/s) by multiplying by a conversion coefficient $\rho_p g / \eta_p$ ($\text{m}^{-1}\text{s}^{-1}$), in which ρ_p and g represent the fluid density (kg/m^3) and acceleration of gravity (9.81 m/s^2), respectively. For water at a temperature of 20 °C, this conversion coefficient is equal to $9.76 \times 10^6 \text{ m}^{-1}\text{s}^{-1}$.

5. Results and discussion

5.1 3D equilibrium distribution of water and gas phases

Following the modelling and simulation procedure described in Section 4.2, the 3D equilibrium distribution of moisture, i.e. liquid-gas mixture in hardened cement paste at various saturation levels can be obtained. Fig. 7 shows the equilibrium distribution of moisture in microstructure and pore network of 7-day old cement paste with water saturation of 50% and 72% respectively, which corresponds to the initial random distribution of moisture as depicted in Fig. 6. The red colour in the figure represents the solid phase consisting of hydration products and anhydrous cement grains. The blue colour and light grey colour stand for the liquid phase and gas phase in pore structure, respectively. As can be seen in Fig. 7, the liquid covers the surface of solid phase and tends to fill the pores with smaller size, while the gas phase tends to occupy the central region of larger pores and forms many gas phase clusters. The liquid-filled pores provide possible paths for water movement and ion transport, while the gas phase clusters act as obstacles to water movement and ion transport but serve as the possible pathways for gas transport, e.g. diffusion of carbon dioxide and oxygen permeation, in unsaturated cementitious materials. It should be pointed out that the used microstructure of cement paste was obtained from X-ray micro-CT, i.e. voxel-based. The limited spatial resolution of CT images may affect the equilibrium distribution of liquid and gas phases in the pore network. In this study, this influence can be roughly ignored, as the equilibrium moisture content is quantified from the number of voxels occupied by liquid and gas phases, respectively.

In order to clearly illustrate the distribution of moisture in pore structure of partially saturated cement paste, the liquid-filled and gas-filled pores are extracted and shown in Figs. 8a and 8b, respectively. It can be seen from Fig. 8a that the liquid-filled pore network is rather complex and comprised of a number of small pores. This can be attributed to the fact that the liquid lies mostly on the surface of solid phase and the network of liquid-filled pores is strongly dependent on the tortuosity of solid surface. In addition, some liquid-filled pores are connected to each other and form a connective liquid-filled pore network from one face of the cube to the opposite face, while the other

liquid-filled pores are isolated from them. In comparison with the liquid-filled pore network, the gas-filled pore network consists of more large pores but less clusters. As the degree of water saturation decreases, more and more pores, in particular, the regions in large pores are gradually occupied by gas phase. Therefore, the 3D equilibrium distribution of liquid and gas phases in cementitious materials depends not only on the degree of water saturation but also on the pore structure and the solid phase in terms of shape, size, connectivity and tortuosity, which are all included in the 3D microstructure of cementitious materials. The obtained 3D equilibrium distribution of moisture in cement paste at various saturation levels can be used as input to estimate the corresponding connectivity of liquid-filled and gas-filled pore network and to simulate the permeation of water and gas in partially saturated cementitious materials, the results of which are presented in the following sections.

Fig. 7 3D equilibrium distribution of liquid and gas phases in 7-day old cement paste: (a) $S_w = 50\%$; (b) $S_w = 72\%$. Red, blue and grey phases represent solid, liquid and gas, respectively

Fig. 8 3D equilibrium distribution of liquid and gas phases in pore structure of 7-day old cement paste with $S_w = 72\%$: (a) Liquid-filled pores; (b) Gas-filled pores

5.2 Connectivity of porous network

Fig. 9 shows the connectivity of liquid-filled pores in cement paste with curing ages of 1, 7 and 28 days as a function of degree of water saturation. Here the degree of connectivity is defined as the ratio of connected liquid-filled pore volume to total liquid-filled pore volume. A degree of connectivity of one means all liquid-filled pores are interconnected to each other. Otherwise, a degree of connectivity of zero manifests that liquid-filled pore space does not form a percolating network any more. The corresponding degree of water saturation is generally referred to as the critical water saturation. It can

be seen that in a fully saturated condition some liquid-filled pores are entirely isolated from the rest of the liquid-filled pores (see Fig. 8a) and the connectivity of liquid-filled pores for cement paste decreases with increasing curing age: from 96% (1 day) to 87% (7 days) and 60% (28 days). This is due to the reduction in porosity and pore size of cement paste with the increase in curing age, which can be seen in Fig. 3. As the water saturation decreases, the connectivity of liquid-filled pores gradually decreases followed by a sharp decline until the critical water saturation is reached. In comparison with cement paste at 1 day of curing, the decreasing tendency in connectivity of liquid-filled pore space at 7 and 28 days is more obvious, which is due to the relatively lower porosity and a more refined pore network with higher proportion of small pores in cement paste at 7 and 28 days compared to those at 1 day. At low water saturation, the liquid-filled pore network becomes more tortuous since the gas phase tends to occupy the central part of larger pores while the liquid phase prefers to cover the solid surface and fill in smaller pores (see Fig. 7). This effect is more pronounced for cement paste at 28 days, as a result of which the connectivity of liquid-filled pore network decreases much more rapidly than that in cement paste at 1 and 7 days of curing. It is worth mentioning that the 3D microstructure of cement paste used in this work was obtained from X-ray micro-CT scans with a limited resolution of $0.5\text{ }\mu\text{m}$. The pores smaller than $0.5\text{ }\mu\text{m}$ cannot be detected and included in the obtained 3D pore structure, which may affect the equilibrium distribution of liquid and gas phases in the pore network at a specific degree of water saturation and the corresponding connectivity of liquid-filled pores and gas-filled pores. In order to overcome such limitation, micro-CT images with a relatively higher resolution are required. This is the subject of ongoing research, the results of which will be presented in future publications.

As seen in Fig. 9, there exist critical water saturations for cement paste with curing ages of 1, 7 and 28 days, which are found to be 35%, 41% and 56%, respectively. This result implies that the critical water saturation is highly associated with the microstructure of cement paste. The specimen with a higher porosity and larger pores but lower tortuosity has higher critical water saturation. By multiplying the critical water saturation by porosity of specimen, the critical liquid-filled porosity can

be obtained. It represents the liquid-filled porosity when the liquid-filled pores are disconnected and the water permeability disappears. It is also known as ‘percolation threshold’. It can be calculated that the values of critical liquid-filled porosity for cement paste with curing ages of 1, 7 and 28 days are 9.6%, 7.7% and 7.6%, respectively. This result is in good agreement with previous findings that the percolation threshold of capillary pores in cementitious materials is about 9% porosity [23, 36].

Fig. 10 shows the connectivity of gas-filled pores in cement paste with curing ages of 1, 7 and 28 days as a function of degree of water saturation. As expected, the connectivity of gas-filled pore network decreases with increasing water saturation: an initial gradual decrease followed by a sharp drop until the critical saturation. Such a change in connectivity for gas-filled pores with water saturation seems to be a little bit more noticeable than that for liquid-filled pores. This can be explained by the difference in the distribution between liquid and gas phases in pore structure of cement paste at various saturation levels. As mentioned above, the gas phase lies in the middle of pores (see Figs. 7 and 8). Thus, it would be easy for gas-filled pores to become isolated as water saturation increases. In contrast, the liquid phase tends to cover the solid surface and typically forms thin layers around the solid surface, as a result of which it would be easier for liquid phase to form continuous paths through the pore space relative to gas phase. In addition, the difference in the connectivity of gas-filled pores between 7 days and 28 days is more apparent than that between 1 day and 7 days over the entire range of water saturation, which indicates that the connectivity of gas-filled pore network is highly dependent on 3D microstructure.

Fig. 9 Connectivity of liquid-filled pores in cement paste with various saturation levels

Fig. 10 Connectivity of gas-filled pores in cement paste with various saturation levels

5.3 Relative water permeability

With the obtained equilibrium distribution of liquid and gas phases in cement paste at various saturation levels, the permeation of water and gas through partially cement paste can be subsequently simulated following the modelling procedure described in Section 4.3. The simulation is run until the steady-state flow condition is reached. Fig. 11 shows the steady-state streamline along the flow direction from bottom to top within 7-day old cement paste at a water saturation of 72%, the corresponding microstructure and liquid-filled pore network of which can be seen in Figs. 4 and 7. It should be pointed out that in the simulation the gas-filled pores, i.e., 28% of total porosity, are classified into impermeable solid-like nodes and act as obstacles for water permeation. As seen in Fig. 11, the water flow is restricted by the impermeable phase composed of anhydrous cement, hydration product and gas, and only passes through the liquid-filled pores. The streamlines have a tortuous configuration and follow the liquid-filled pore network. In addition, it can be observed from the velocity distribution shown in Fig. 11b that the flow velocity at some positions (i.e., in dark red) is obviously greater than that in other regions. These positions probably correspond to the small liquid-filled pores. This result clearly indicates the flow velocity distribution in partially saturated cement paste is highly related to the liquid-filled pore size distribution. Furthermore, it indicates the LB method used in this study provides insight into the internal velocity distribution at the pore scale and allows one to detect preferential flow paths within the specimen with various degrees of water saturation. Therefore, the LB simulation offers a significant potential for new fundamental insights and comprehensive understanding of fluid flow processes in cementitious materials over the whole range of saturation.

Based on the simulated steady-state flow velocity, the intrinsic permeability in LB units, κ_{lb} , can be calculated according to Eq. 17 and then converted to intrinsic permeability in physical units (m^2), κ . Fig. 12 shows the intrinsic water permeability of cement paste with curing ages of 1, 7 and 28 days as a function of effective liquid-filled porosity, which is equal to liquid-filled porosity of cement paste specimen multiplied by connectivity of liquid-filled pores related to water saturation, as discussed in the previous section. As expected, the intrinsic water permeability decreases with the decrease in

effective liquid-filled porosity. The decrease in intrinsic permeability is initially stable but becomes more pronounced when the effective liquid-filled porosity is relatively low and approaches the percolation threshold. At the same effective liquid-filled porosity, the intrinsic water permeability of cement paste at different ages of curing is found to be very close to each other. Moreover, it can be observed that there exists a strong correlation between the intrinsic water permeability and effective liquid-filled porosity regardless of curing age of cement paste. This result is in consistent with the previous findings for cementitious materials that there is clearly a unique relationship between the water permeability and effective porosity [22].

It should be mentioned that the simulated intrinsic water permeability of saturated specimens seems to be 2 or 3 times higher than experimental data from literature shown in [18, 22, 37]. This can be attributed to the fact that (i) the saturation conditions of specimens in simulations and experiments are generally not the same. In practice, it is difficult if not impossible to realize a full saturation state and the specimens for laboratory permeability testing may not be fully saturated [20]. (ii) the permeability tests usually last several days or weeks or even months to reach a steady-state flow condition. During this period, the cement hydration proceeds and microstructure changes. Thus, the ages of specimens for simulations are not exactly the same with those of specimens achieving steady-state flow conditions for measurements. Therefore, the water permeability measured in the experiments should be underestimated, especially in the later stage [22]. (iii) the experimental data of water permeability of cement pastes from literature show significant variation (see [18, 22, 37]) due to the differences in their microstructures. In this study, the emphasis is placed on the estimation of the influence of water saturation levels on water permeability of cement paste. The relative water permeability, κ_{rw} , which is defined as the ratio of the intrinsic water permeability at a certain degree of water saturation (S_w) to the intrinsic water permeability in a fully saturated condition ($S_w = 100\%$), is used to investigate the effect of water saturation in a quantitative manner. Fig. 13 shows the relative water permeability of cement paste as a function of water saturation. For cement paste with various curing ages, there is a significant drop in relative water permeability when the water saturation

decreases from 100% to around 70%. This is followed by a less dramatic variation in relative water permeability with water saturation until the critical water saturation at which there is no connected liquid-filled pore network allowing water to pass through and the water permeability goes to zero. The dependence of relative water permeability on water saturation for cement paste at different curing ages is slightly different, which can be ascribed to the different microstructure, particularly pore structure, of cement paste at different curing ages. The relative water permeability of 28-day old cement paste is more sensitive to a change in water saturation than that of cement paste at 1 and 7 days of curing. The reason for this is that 28-day old cement paste has a lower porosity and contains denser, less interconnected and more tortuous pore network, as a result of which the connectivity of liquid-filled pores in 28-day old cement paste is more significantly affected by water saturation, as shown in Fig. 9. All these indicate that water permeability of cement paste at various saturation states is highly dependent on the 3D microstructure of cement paste.

For the purpose of validation, the experimental data obtained by Kameche et al. [5] are used and plotted together with the simulation results in Fig. 13. It should be noted that there are only a very limited number of experimental studies on water permeability of partially saturated cementitious materials available due to the difficulty of measurement. In their experiment, the evolution of water permeability with the degree of water saturation was measured using ten concrete specimens with the same size from the same batch. A significant influence of water saturation on relative water permeability was observed, which is consistent with the simulations here. Although the specimens used in the simulations in this study are not exactly the same as those in their experiment, there is a very good agreement between the simulation results and their experimental data that the relative water permeability against water saturation follows a nonlinear (exponential or polynomial) trend curve with a satisfactory correlation coefficient. In addition, when the water saturation approached around 40%, the liquid water phase tended to be disconnected and the water permeability became very close to zero. This finding agrees very well with the simulation results that the critical water saturation is approximately 40% (see Figs. 9 and 13 for cement paste with curing ages of 1 and 7 days).

Fig. 11 Steady-state water flow in 7-day old cement paste with $S_w = 72\%$: (a) Streamline; (b)

Velocity distribution

Fig. 12 Intrinsic water permeability of cement paste against effective liquid-filled porosity

Fig. 13 Relative water permeability of cement paste with curing ages of 1, 7 and 28 days

5.4 Relative gas permeability

Following a same modelling and simulation procedure as mentioned above, the intrinsic gas permeability of cement paste with various curing ages over the whole range of saturation can be obtained. Fig. 14 shows the intrinsic gas permeability against effective gas-filled porosity, which is determined by multiplying gas-filled porosity by connectivity of gas-filled pores at each water saturation state (see Fig. 10). Note that the gas permeability of cement paste is strongly dependent on the effective gas-filled porosity. The intrinsic gas permeability decreases as the water saturation increases and the effective gas-filled porosity decreases. When the effective gas-filled porosity is less than 2%, the intrinsic gas permeability tends to be very sensitive to effective gas-filled porosity. The reason for this is that the tortuosity of pore network is significantly influenced by effective porosity including porosity and pore connectivity. When the effective porosity is close to zero, the pore network would be complex and highly tortuous. As a result, it becomes difficult for fluid flow to permeate through such pore network and the fluid permeability would decrease sharply. Besides these, a unique relationship between the intrinsic gas permeability and effective gas-filled porosity being independent of curing age of cement paste can be observed. This result is similar to that for intrinsic water permeability as discussed above and further implies that the effective porosity plays a critical role in the estimation of fluid permeability.

Fig. 15 shows the relative gas permeability, that is defined as the ratio between the intrinsic gas permeability at a certain saturation (S_w) and the intrinsic gas permeability in a fully dry condition ($S_w = 0\%$), of cement paste at various curing ages as a function of water saturation. It can be seen that the relative gas permeability is highly influenced by water saturation. As the water saturation increases, there is a sharp decrease in the relative gas permeability for cement paste with various curing ages. Compared to cement paste at 1 and 7 days, the decrease in relative gas permeability of 28-day old cement paste with increasing water saturation is more noticeable due to its relatively lower porosity, less interconnected and more tortuous gas-filled pore network at each saturation level, as shown in Fig. 10.

As a comparison, the available experimental data of gas permeability of partially saturated concrete in the literature [5, 6, 38] are used and expressed in terms of relative gas permeability, which are also shown in Fig. 15. It is worth pointing out that the experimental data given in [38] were collected from [11, 39-42]. The simulation results show a general satisfactory agreement with the experimental data. It should be highlighted that the measured values of relative gas permeability obtained by different authors show a large variation. This can be explained by the different specimens they prepared and used for measurements, the microstructures of which would be not the same. This finding provides further support for one of the main conclusions of this study that the fluid permeability of unsaturated cementitious materials is strongly dependent on their microstructures.

Fig. 14 Intrinsic gas permeability of cement paste against effective gas-filled porosity

Fig. 15 Relative gas permeability of cement paste with curing ages of 1, 7 and 28 days

6. Conclusions

In this paper, an integrated modelling approach comprised of modified Shan-Chen multiphase lattice Boltzmann model, cluster-labelling algorithm and single-phase multi-relaxation-time lattice

Boltzmann model is presented to estimate the permeability of partially saturated cementitious materials. Firstly, the distribution of moisture (a mixture of liquid and gas) in 3D microstructures of cement paste obtained by high-resolution X-ray micro-CT over the full range of water saturation is simulated using a multiphase lattice Boltzmann model. Subsequently, the connectivity of liquid-filled and gas-filled pore network at each saturation level is quantified. Finally, the multi-relaxation-time lattice Boltzmann model is applied to simulate the water and gas flow through partially saturated cement pastes and obtain the corresponding water permeability and gas permeability. The influences of degree of water saturation and microstructure on permeability of cement paste are then investigated in a quantitative manner. Based on the findings of this study, the following conclusions can be drawn:

- At a certain degree of water saturation, the liquid phase covers the surface of solid phase and tends to fill the pores with smaller size, while the gas phase tends to occupy the central region of larger pores and forms many gas phase clusters. In addition, the distribution of liquid and gas in unsaturated cementitious materials depends not only on pore size but also on solid phase in terms of shape, size, connectivity and tortuosity, which are all included in the 3D microstructure of cementitious materials.
- There exists a critical water saturation at which the liquid-filled or gas-filled capillary porosity becomes disconnected. The critical water saturation is highly associated with microstructure. For cement paste with curing ages of 1, 7 and 28 days, the critical water saturations are found to be 35%, 41% and 56%, respectively.
- The degree of water saturation has a significant influence on both water permeability and gas permeability of cement paste with various curing ages. As degree of water saturation decreases, there is a gradual drop in water permeability followed by a sharp decrease when the water saturation level is approaching the critical water saturation. For all specimens, there exists a strong correlation between water (gas) permeability and effective water (gas) filled capillary porosity, which implies that effective porosity play a critical role in the estimation of transport properties of cementitious materials.

- The permeability of cementitious materials at various saturation states is strongly dependent on their 3D microstructures. The change in water (gas) permeability of 28-day old cement paste is more sensitive to a change in water saturation than that of cement paste at 1 and 7 days of curing. This is attributed to the relatively lower porosity, and denser, less interconnected and more tortuous pore network in 28-day old cement paste.
- The simulated water permeability and gas permeability of cementitious materials as a function of water saturation show very good agreement with experimental data in the literature.

Acknowledgements

The financial support from the Royal Society and the National Natural Science Foundation of China via an international exchange grant IE150587 is gratefully acknowledged.

References

- [1] V. Baroghel-Bouny, T.Q. Nguyen, P. Dangla, Assessment and prediction of RC structure service life by means of durability indicators and physical/chemical models, *Cement Concrete Comp*, 31 (2009) 522-534.
- [2] Y. Zhang, M. Zhang, Transport properties in unsaturated cement-based materials - A review, *Constr Build Mater*, 72 (2014) 367-379.
- [3] A. Abbas, M. Carcasses, J.P. Ollivier, Gas permeability of concrete in relation to its degree of saturation, *Mater Struct*, 32 (1999) 3-8.
- [4] C. Galle, J.F. Daian, Gas permeability of unsaturated cement-based materials: application of a multi-scale network model, *Mag Concrete Res*, 52 (2000) 251-263.
- [5] Z.A. Kameche, F. Ghomari, M. Choinska, A. Khelidj, Assessment of liquid water and gas permeabilities of partially saturated ordinary concrete, *Constr Build Mater*, 65 (2014) 551-565.
- [6] J.P. Monlouis-Bonnaire, J. Verdier, B. Perrin, Prediction of the relative permeability to gas flow of cement-based materials, *Cement Concrete Res*, 34 (2004) 737-744.
- [7] G. Wardeh, B. Perrin, Relative permeabilities of cement-based materials: Influence of the tortuosity function, *J Build Phys*, 30 (2006) 39-57.
- [8] S. Zamani, R.M. Kowalczyk, P.J. McDonald, The relative humidity dependence of the permeability of cement paste measured using GARField NMR profiling, *Cement Concrete Res*, 57 (2014) 88-94.
- [9] Y. Mualem, New Model for Predicting Hydraulic Conductivity of Unsaturated Porous-Media, *Water Resour Res*, 12 (1976) 513-522.
- [10] M.T. Van Genuchten, A Closed-Form Equation for Predicting the Hydraulic Conductivity of Unsaturated Soils, *Soil Sci Soc Am J*, 44 (1980) 892-898.
- [11] V. Baroghel-Bouny, Water vapour sorption experiments on hardened cementitious materials. Part II: Essential tool for assessment of transport properties and for durability prediction, *Cement Concrete Res*, 37 (2007) 438-454.
- [12] C. Zhou, Predicting water permeability and relative gas permeability of unsaturated cement-based material from hydraulic diffusivity, *Cement Concrete Res*, 58 (2014) 143-151.
- [13] C. Zhou, W. Chen, W. Wang, F. Skoczyłas, Unified determination of relative molecular diffusivity and fluid permeability for partially saturated cement-based materials, *Cement Concrete Res*, 67 (2015) 300-309.

- [14] C. Zhou, W. Chen, W. Wang, F. Skoczylas, Indirect assessment of hydraulic diffusivity and permeability for unsaturated cement-based material from sorptivity, *Cement Concrete Res*, 82 (2016) 117-129.
- [15] N.S. Martys, Diffusion in partially-saturated porous materials, *Mater Struct*, 32 (1999) 555-562.
- [16] N.S. Martys, J.G. Hagedorn, Multiscale modeling of fluid transport in heterogeneous materials using discrete Boltzmann methods, *Mater Struct*, 35 (2002) 650-658.
- [17] C. Pan, M. Hilpert, C.T. Miller, Lattice-Boltzmann simulation of two-phase flow in porous media, *Water Resour Res*, 40 (2004) W01501.
- [18] M. Zalzale, P.J. McDonald, Lattice Boltzmann simulations of the permeability and capillary adsorption of cement model microstructures, *Cement Concrete Res*, 42 (2012) 1601-1610.
- [19] M. Zalzale, P.J. McDonald, K.L. Scrivener, A 3D lattice Boltzmann effective media study: understanding the role of C-S-H and water saturation on the permeability of cement paste, *Model Simul Mater Sc*, 21 (2013) 085016
- [20] K. Li, M. Stroeven, P. Stroeven, L.J. Sluys, Investigation of liquid water and gas permeability of partially saturated cement paste by DEM approach, *Cement Concrete Res*, 83 (2016) 104-113.
- [21] M. Zhang, G. Ye, K. van Breugel, Modeling of ionic diffusivity in non-saturated cement-based materials using lattice Boltzmann method, *Cement Concrete Res*, 42 (2012) 1524-1533.
- [22] M. Zhang, G. Ye, K. van Breugel, Microstructure-based modeling of permeability of cementitious materials using multiple-relaxation-time lattice Boltzmann method, *Comp Mater Sci*, 68 (2013) 142-151.
- [23] M. Zhang, Y. He, G. Ye, D.A. Lange, K. van Breugel, Computational investigation on mass diffusivity in Portland cement paste based on X-ray computed microtomography (mu CT) image, *Constr Build Mater*, 27 (2012) 472-481.
- [24] M. Zhang, A.P. Jivkov, Microstructure-informed modelling of damage evolution in cement paste, *Constr Build Mater*, 66 (2014) 731-742.
- [25] M. Zhang, A.P. Jivkov, Micromechanical modelling of deformation and fracture of hydrating cement paste using X-ray computed tomography characterisation, *Compos Part B-Eng*, 88 (2016) 64-72.
- [26] M. Zhang, G. Ye, K. van Breugel, A numerical-statistical approach to determining the representative elementary volume (REV) of cement paste for measuring diffusivity, *Mater Construcc*, 60 (2010) 7-20.
- [27] Y. Qian, D. Dhumieres, P. Lallemand, Lattice Bgk Models for Navier-Stokes Equation, *Europhys Lett*, 17 (1992) 479-484.
- [28] D. d'Humieres, I. Ginzburg, M. Krafczyk, P. Lallemand, L. Luo, Multiple-relaxation-time lattice Boltzmann models in three dimensions, *Philosophical Transactions of the Royal Society of London Series a-Mathematical Physical and Engineering Sciences*, 360 (2002) 437-451.
- [29] X. Shan, H. Chen, Lattice Boltzmann Model for Simulating Flows with Multiple Phases and Components, *Phys Rev E*, 47 (1993) 1815-1819.
- [30] P.J. McDonald, M.N. Turner, Combining effective media and multi-phase methods of Lattice Boltzmann modelling for the characterisation of liquid-vapour dynamics in multi-length scale heterogeneous structural materials, *Model Simul Mater Sc*, 24 (2016) 015010.
- [31] X. Shan, H. Chen, Simulation of Nonideal Gases and Liquid-Gas Phase-Transitions by the Lattice Boltzmann-Equation, *Phys Rev E*, 49 (1994) 2941-2948.
- [32] P. Yuan, L. Schaefer, Equations of state in a lattice Boltzmann model, *Phys Fluids*, 18 (2006).
- [33] R. Benzi, L. Biferale, M. Sbragaglia, S. Succi, F. Toschi, Mesoscopic modeling of a two-phase flow in the presence of boundaries: The contact angle, *Phys Rev E*, 74 (2006).
- [34] Y.K. Suh, J. Kang, S. Kang, Assessment of algorithms for the no-slip boundary condition in the lattice Boltzmann equation of BGK model, *Int J Numer Meth Fl*, 58 (2008) 1353-1378.
- [35] Q. Zou, X. He, On pressure and velocity boundary conditions for the lattice Boltzmann BGK model, *Phys Fluids*, 9 (1997) 1591-1598.
- [36] G. Ye, Percolation of capillary pores in hardening cement pastes, *Cement Concrete Res*, 35 (2005) 167-176.

- [37] Z. Zhang, M. Thiery, V. Baroghel-Bouny, Investigation of moisture transport properties of cementitious materials, *Cement Concrete Res*, 89 (2016) 257-268.
- [38] H. Ranaivomanana, J. Verdier, A. Sellier, X. Bourbon, Prediction of relative permeabilities and water vapor diffusion reduction factor for cement-based materials, *Cement Concrete Res*, 48 (2013) 53-63.
- [39] V. Baroghel-Bouny, M. Mainguy, T. Lassabatere, O. Coussy, Characterization and identification of equilibrium and transfer moisture properties for ordinary and high-performance cementitious materials, *Cement Concrete Res*, 29 (1999) 1225-1238.
- [40] H. Ranaivomanana, J. Verdier, A. Sellier, X. Bourbon, Toward a better comprehension and modeling of hysteresis cycles in the water sorption-desorption process for cement based materials, *Cement Concrete Res*, 41 (2011) 817-827.
- [41] G. Villain, V. Baroghel-Bouny, C. Kounkou, C. Hua, Mesure de la perméabilité aux gaz en fonction du taux de saturation des bétons, *Rev Fr Génie Civ*, 5 (2001) 251-268.
- [42] M. Thiery, V. Baroghel-Bouny, N. Bourneuf, G. Villain, C. Stéfani, Modélisation du séchage des bétons. Analyse des différents modes de transfert hydrique, *Rev Eur Génie Civ*, 11 (2007) 541-577.

Figures

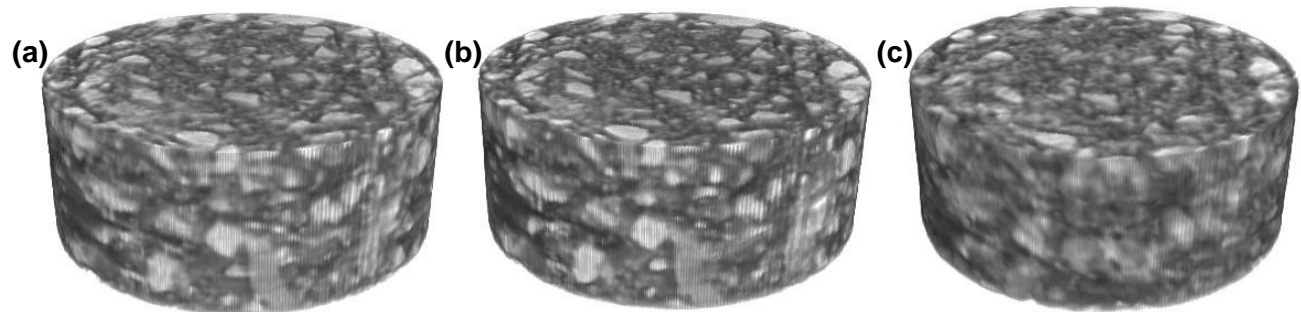


Fig. 1 Micro-CT images of hydrating cement pastes with 200 μm in diameter and 100 μm in thickness with curing ages of (a) 1 day; (b) 7 days; (c) 28 days. The dark, grey and white phases represent capillary pore, hydration product and anhydrous cement grain, respectively

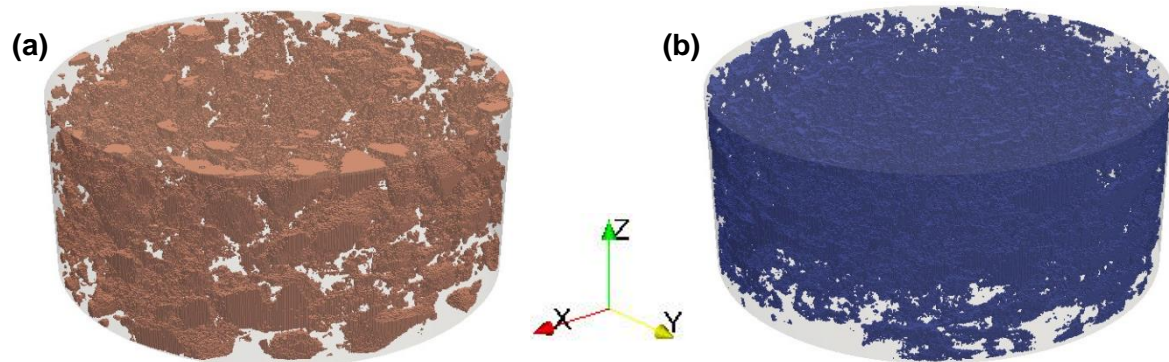


Fig. 2 Different phases in 7-day old cement paste: (a) Anhydrous cement grains; (b) Capillary pores

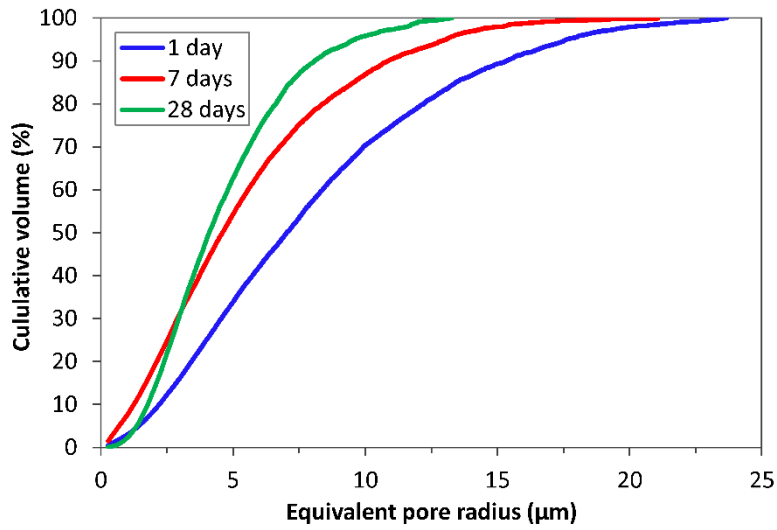


Fig. 3 Pore size distribution of cement paste with curing ages of 1, 7 and 28 days

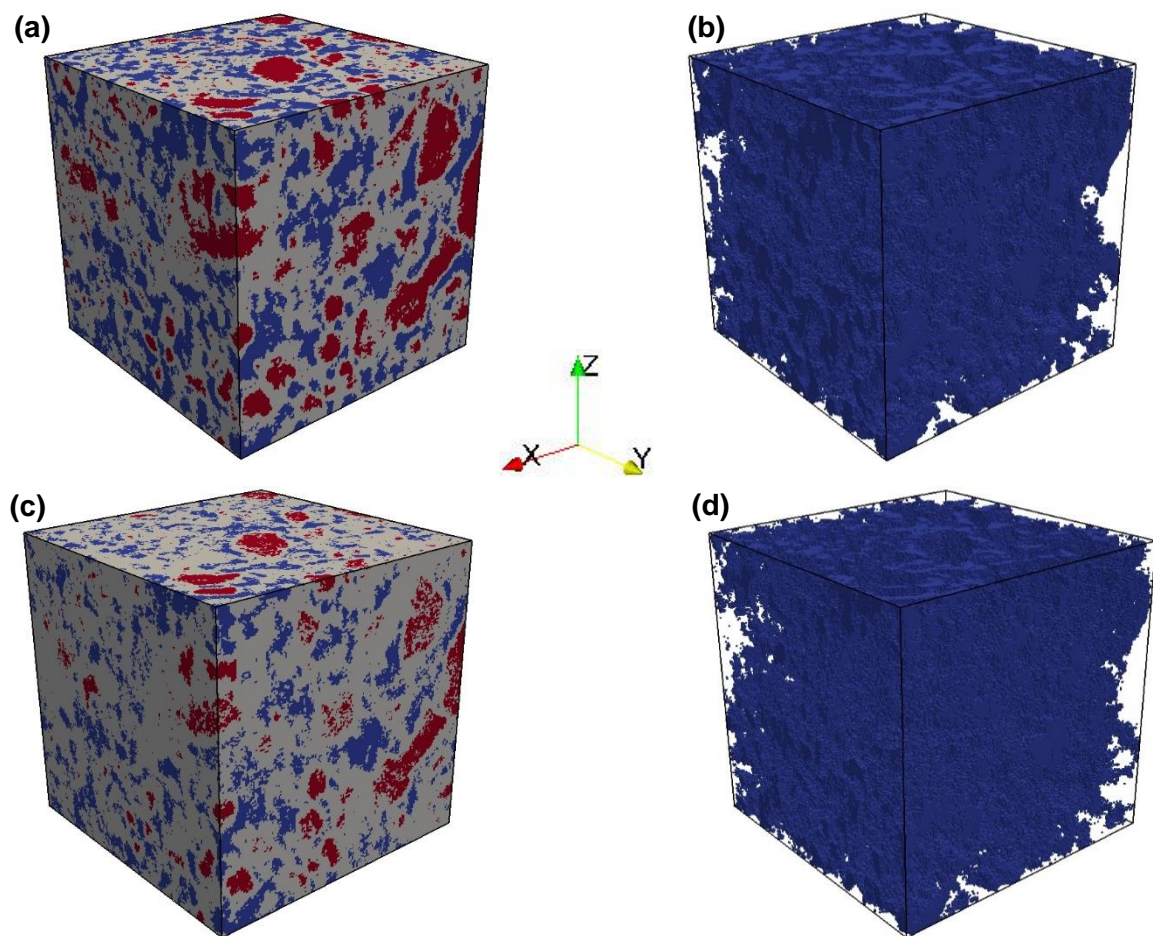


Fig. 4 Hardened cement paste with $100 \times 100 \times 100 \mu\text{m}^3$: (a) Microstructure at 1 day; (b) Pore structure at 1 day; (c) Microstructure at 7 days; (d) Pore structure at 7 days. Red, light grey and blue regions denote anhydrous cement grain, hydration product and capillary pore, respectively

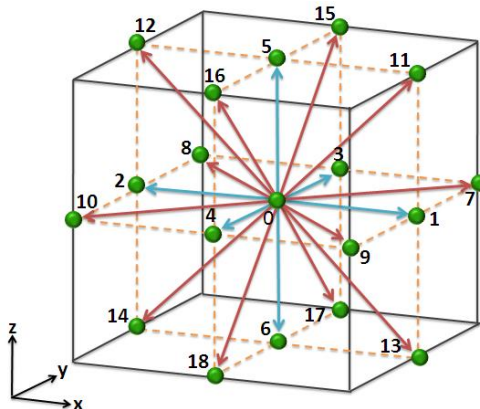


Fig. 5 Lattice velocity direction of the D3Q19 lattice Boltzmann model

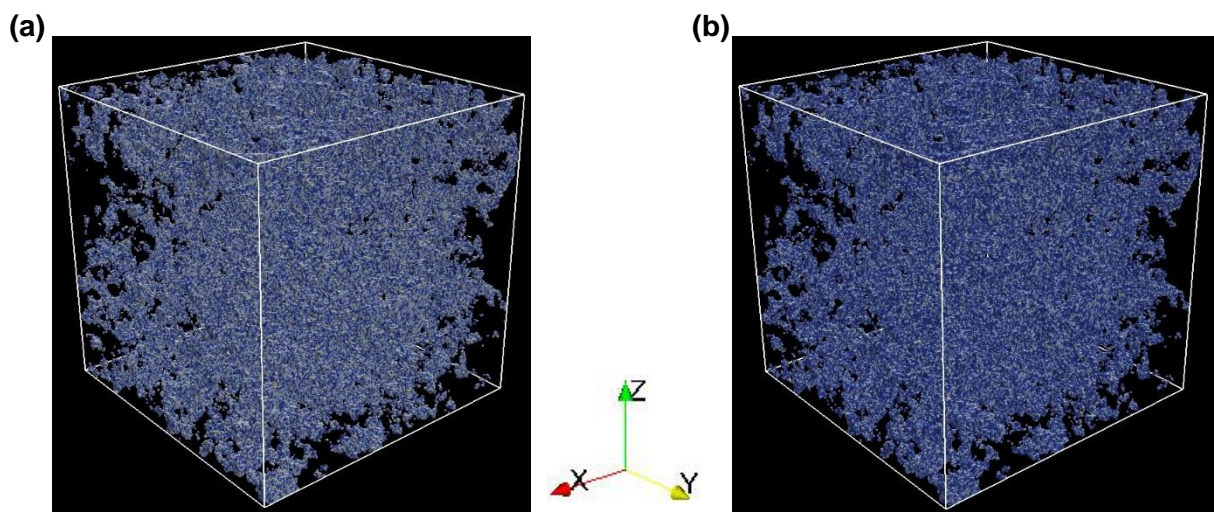


Fig. 6 Initial random distribution of liquid and gas phases in pore structure of 7-day old cement paste: (a) $S_w = 50\%$; (b) $S_w = 72\%$. Blue and grey phases represent liquid and gas, respectively

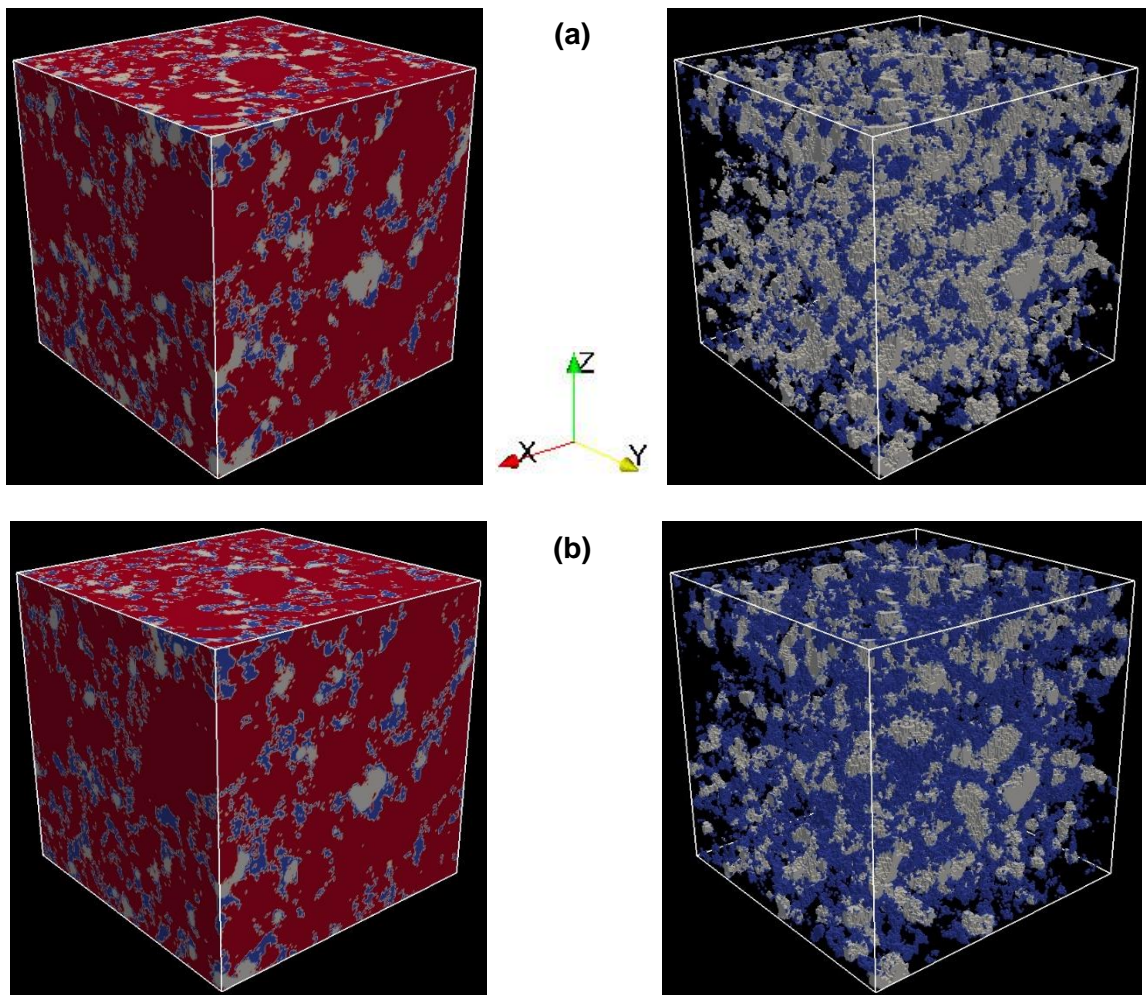


Fig. 7 3D equilibrium distribution of liquid and gas phases in 7-day old cement paste: (a) $S_w = 50\%$; (b) $S_w = 72\%$. Red, blue and grey phases represent solid, liquid and gas, respectively

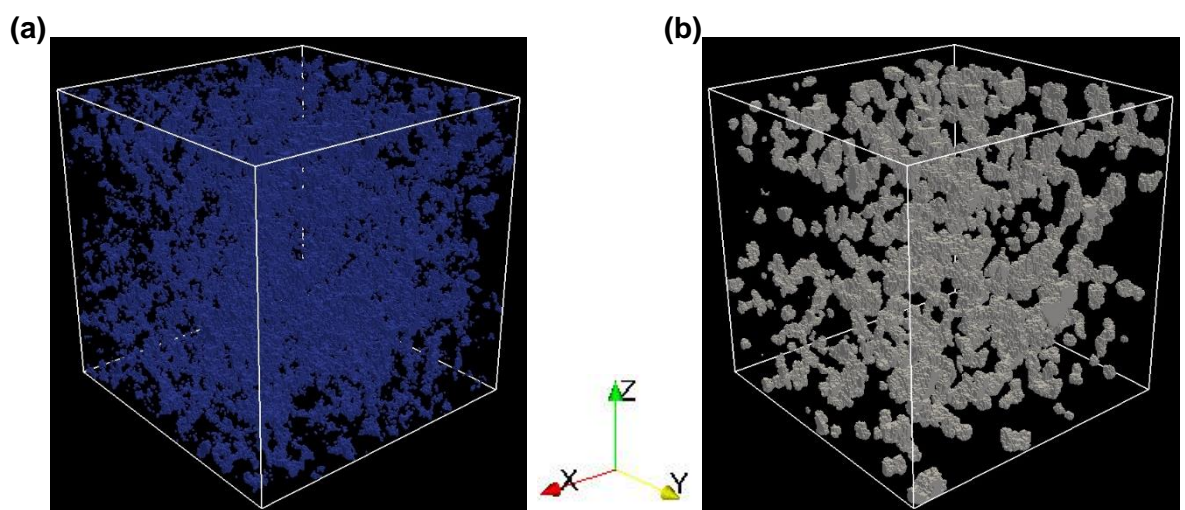


Fig. 8 3D equilibrium distribution of liquid and gas phases in pore structure of 7-day old cement paste with $S_w = 72\%$: (a) Liquid-filled pores; (b) Gas-filled pores

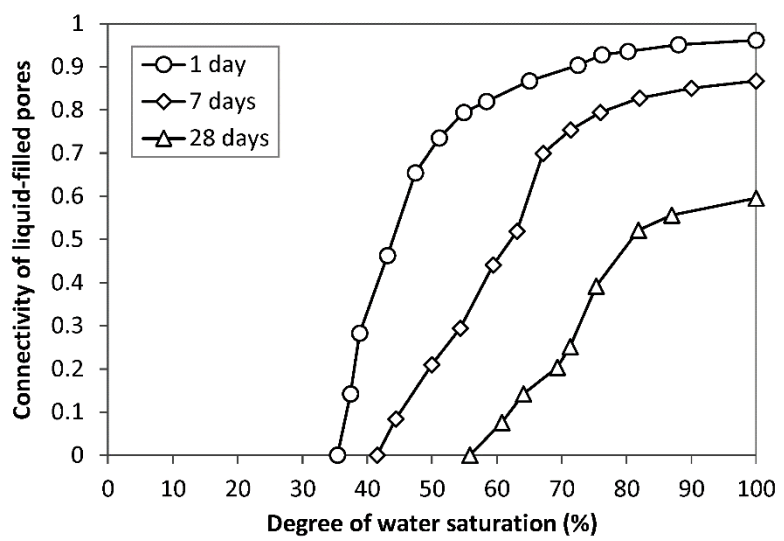


Fig. 9 Connectivity of liquid-filled pores in cement paste with various saturation levels

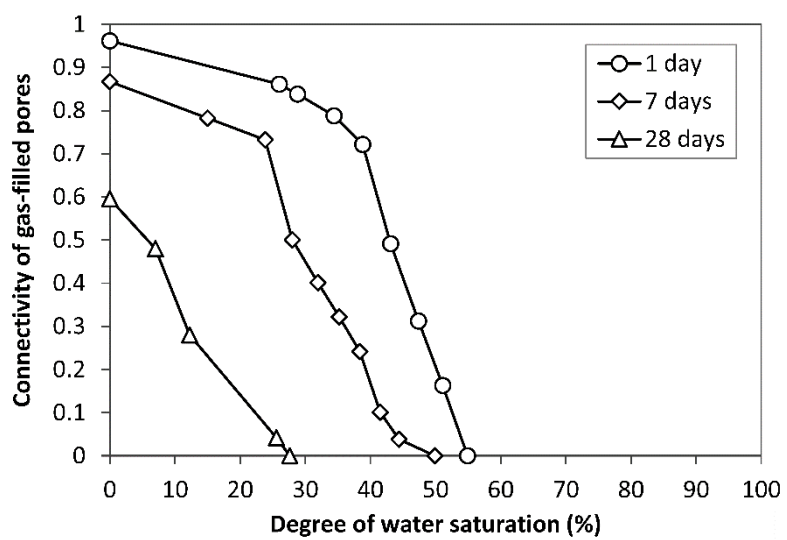


Fig. 10 Connectivity of gas-filled pores in cement paste with various saturation levels

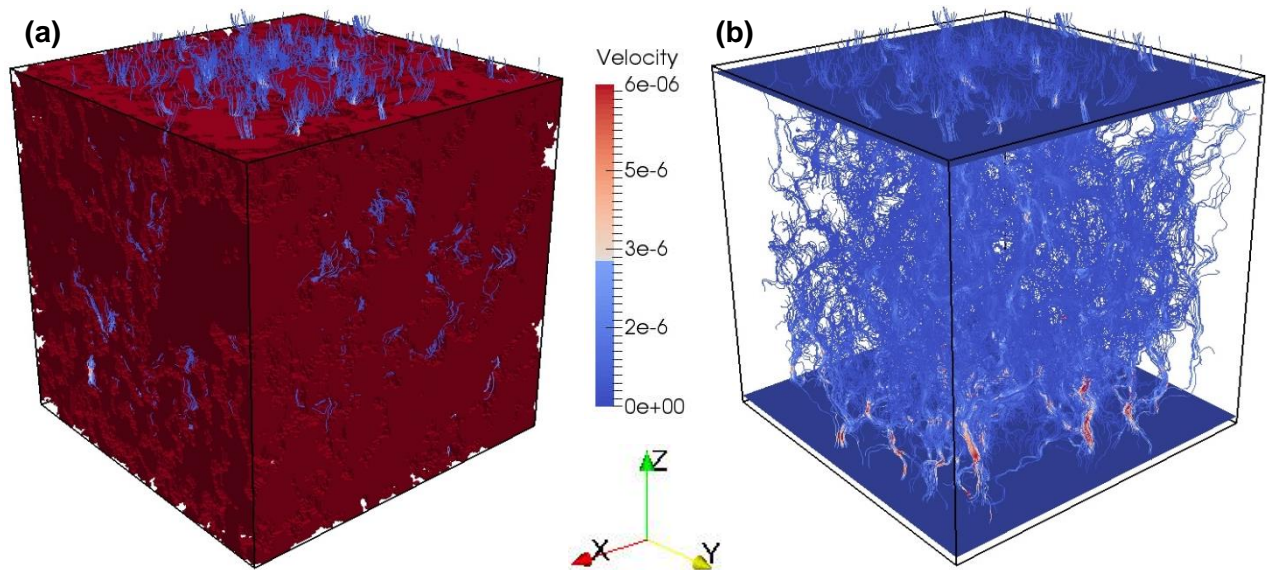


Fig. 11 Steady-state water flow in 7-day old cement paste with $S_w = 72\%$: (a) Streamline; (b) Velocity distribution

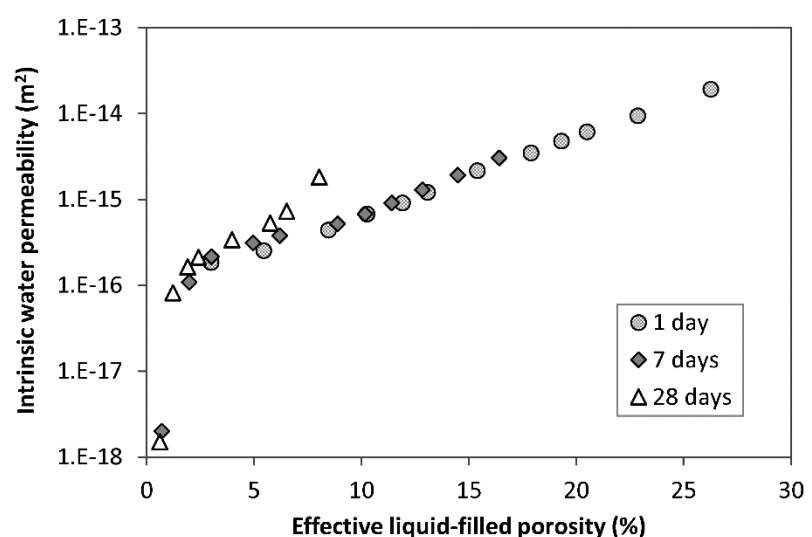


Fig. 12 Intrinsic water permeability of cement paste against effective liquid-filled porosity

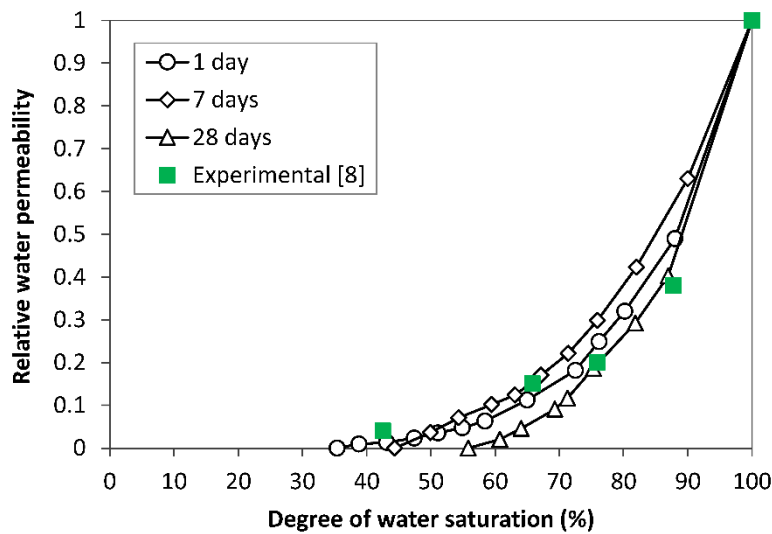


Fig. 13 Relative water permeability of cement paste with curing ages of 1, 7 and 28 days

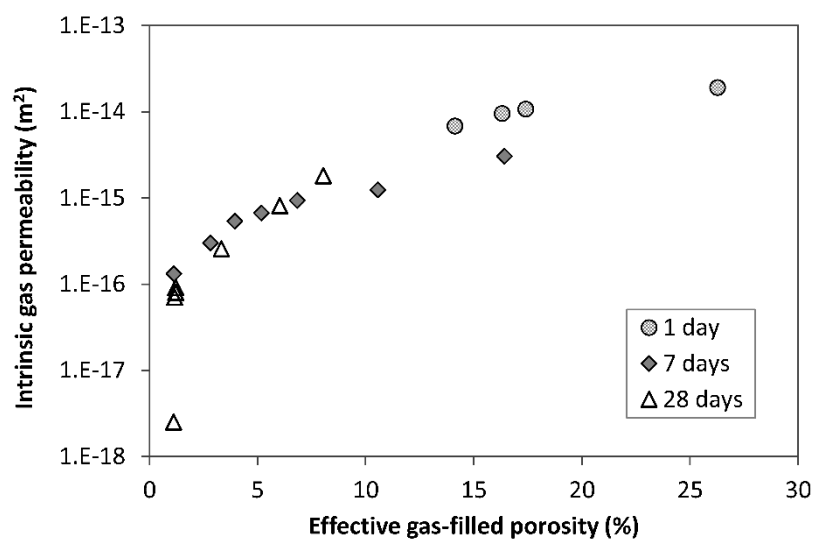


Fig. 14 Intrinsic gas permeability of cement paste against effective gas-filled porosity

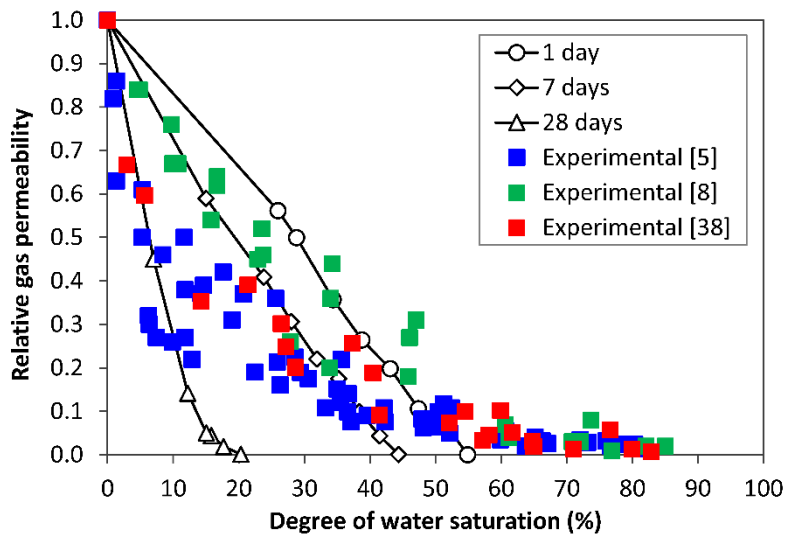


Fig. 15 Relative gas permeability of cement paste with curing ages of 1, 7 and 28 days